Journal of Controlled Release 217 (2015) 92–101

Contents lists available at ScienceDirect

Journal of Controlled Release

journal homepage: www.elsevier.com/locate/jconrel

A corrole nanobiologic elicits tissue-activated MRI contrast enhancement and tumor-targeted toxicity

Jessica D. Sims [a], Jae Youn Hwang [d], Shawn Wagner [a,b], Felix Alonso-Valenteen [a], Chris Hanson [a], Jan Michael Taguiam [a], Richard Polo [a], Ira Harutyunyan [e], Gevorg Karapetyan [e], Karn Sorasaenee [e], Ahmed Ibrahim [a,c], Eduardo Marban [c], Rex Moats [e], Harry B. Gray [f], Zeev Gross [g], Lali K. Medina-Kauwe [a,h,*]

[a] Department of Biomedical Sciences, Cedars-Sinai Medical Center, Los Angeles, CA, USA
[b] Biomedical Imaging Research Institute, Cedars-Sinai Medical Center, Los Angeles, CA, USA
[c] Heart Institute, Cedars-Sinai Medical Center, Los Angeles, CA, USA
[d] Daegu Gyeongbuk Institute of Science & Technology, Daegu, Republic of Korea
[e] Translational Biomedical Imaging Laboratory, Department of Radiology, The Saban Reseach Institute, Children's Hospital, Keck Medical School of USC, Los Angeles, USA
[f] Department of Chemistry, California Institute of Technology, Pasadena, CA, USA
[g] Schulich Faculty of Chemistry, Technion-Israel Institute, Haifa, Israel
[h] Geffen School of Medicine, University of California-Los Angeles, USA

ARTICLE INFO

Article history:
Received 23 April 2015
Received in revised form 10 August 2015
Accepted 24 August 2015
Available online 31 August 2015

Keywords:
Nanoparticle
Tumor-targeting
Corrole
Manganese
MRI

ABSTRACT

Water-soluble corroles with inherent fluorescence can form stable self-assemblies with tumor-targeted cell penetration proteins, and have been explored as agents for optical imaging and photosensitization of tumors in pre-clinical studies. However, the limited tissue-depth of excitation wavelengths limits their clinical applicability. To examine their utility in more clinically-relevant imaging and therapeutic modalities, here we have explored the use of corroles as contrast enhancing agents for magnetic resonance imaging (MRI), and evaluated their potential for tumor-selective delivery when encapsulated by a tumor-targeted polypeptide. We have found that a manganese-metallated corrole exhibits significant T1 relaxation shortening and MRI contrast enhancement that is blocked by particle formation in solution but yields considerable MRI contrast after tissue uptake. Cell entry but not low pH enables this. Additionally, the corrole elicited tumor-toxicity through the loss of mitochondrial membrane potential and cytoskeletal breakdown when delivered by the targeted polypeptide. The protein–corrole particle (which we call HerMn) exhibited improved therapeutic efficacy compared to current targeted therapies used in the clinic. Taken together with its tumor-preferential biodistribution, our findings indicate that HerMn can facilitate tumor-targeted toxicity after systemic delivery and tumor-selective MR imaging activatable by internalization.

1. Introduction

Multifunctional therapeutics, or "theranostics", combine several activities such as imaging, diagnostic, or therapeutic functions into a single complexed particle, thus providing a powerful approach to simultaneously detecting, diagnosing, and treating disease [1,2]. Engineering a theranostic commonly entails chemically conjugating different agents to a scaffold, such as a polymer, with each agent imparting a different function (*i.e.* tissue or cell targeting, membrane penetration, drug delivery, imaging). A potential complication with such approaches is the requirement for multiple covalent coupling reactions that increase the complexity and heterogeneity of the complex, and may abrogate the activities of its separate components. Sulfonated corroles can overcome this complication because they can non-covalently assemble with protein-based delivery agents while bearing potential theranostic functions, thus forming a multifunctional particle from only two components.

Sulfonated corroles are macrocyclic molecules with structural similarity to porphyrins and bear several notable characteristics that lend to their use as multifunctional payloads. The amphiphilicity of sulfonated corroles contributes to their water-solubility and tight non-covalent binding to proteins [3–5], thus enabling rapid assembly with carrier proteins and delivery in physiological conditions. The net negative charge of sulfonated corroles prevents their penetration into cells in the absence of a membrane-lytic molecule [3], thus enabling selective cell entry directed by the delivery agent. The incorporation of a metal ligand in the corrole ring can contribute to imaging and therapeutic potential. For example, non-metallated and gallium(III)-metallated corroles are both cytotoxic and intensely fluorescent [3–5], whereas iron(III) and manganese(III)-metallated corroles are non-fluorescent and have exhibited robust antioxidant activity on neuronal tissue [6].

* Corresponding author at: Department of Biomedical Sciences, Cedars-Sinai Medical Center, 8700 Beverly Blvd., Davis 3065, Los Angeles, CA 90048, USA.
E-mail address: Medinal@cshs.org (L.K. Medina-Kauwe).

http://dx.doi.org/10.1016/j.jconrel.2015.08.046
0168-3659/

Whereas fluorescent corroles have been examined as agents for optical imaging of tumors in mice [7] and photosensitization of tumor cells *in vitro* [8,9], the limited tissue-depth of excitation wavelengths limits their clinical applicability. To assess the feasibility of using more clinically-relevant imaging modalities, here we explored the utility of corroles as contrast enhancing agents for magnetic resonance imaging (MRI), thus expanding the theranostics benefits inherent to the corroles.

In the current study, a comparison of *in vitro* T1 relaxation shortening and MRI contrast enhancement activities between sulfonated gallium(III), iron(III), and manganese(III)-metallated corroles singled out the manganese (Mn) compound as a candidate for further evaluation in the context of a tumor-targeted particle. Assembly of the particle, HerMn, resulted from binding of the Mn-corrole (or S2Mn) with the recombinant protein, HerPBK10. The peptide domains comprising HerPBK10 impart functions that can facilitate the targeted delivery (through binding to the human epidermal growth factor receptor or HER) and cell entry of membrane-impermeant molecules [10–13]. Importantly, HER2-3 heterodimers, which are recognized by the heregulin-derived targeting ligand of HerPBK10, are predominantly displayed on HER2 + tumors [14], hence targeting is preferential to HER2 + tumor cells [11,13,15]. In agreement, we have shown elsewhere that HerPBK10 can mediate preferential targeting *in vivo* to tumors expressing relatively higher HER2-3 levels in comparison to tumors expressing low/negligible levels of these receptor subunits [15].

Here we present evidence that the sulfonated Mn(III) corrole can elicit MRI contrast enhancement as well as tumor-selective toxicity when delivered by HerPBK10. The tumor-toxic activity comes somewhat as a surprise given the cytoprotective effects that this corrole has exhibited previously on non-tumor, specifically neuronal, tissue [6]. Hence, in this study, we also probe the mechanism of tumor-cell toxicity elicited by the Mn-corrole, and compare therapeutic efficacy *in vitro* against current targeted and non-targeted therapies used in the clinic. Finally, interrogating the MRI capability of protein-bound *vs.* free corrole yielded findings suggesting that contrast enhancement in tissue is activated by pH-independent mechanisms relying on cell uptake.

2. Materials and methods

2.1. Materials

The recombinant fusion protein, HerPBK10 (comprised of the receptor-binding domain of heregulin-α fused to the adenovirus penton base modified by a carboxy-terminal decalysine tail) [16], was produced and isolated from a bacterial expression system as described previously [13]. S2Mn (chemical structure shown in Fig. 1A) was synthesized, reconstituted in phosphate-buffered saline (PBS), and quantified as described previously [3]. HerMn complexes were assembled non-covalently by combining HerPBK10 and S2Mn as described [10]. Briefly, S2Mn and HerPBK10 were mixed at a corrole:protein ratio of 30:1 (the maximum number of corrole molecules bound per HerPBK10 protein, as determined previously) [3,11] in PBS and agitated gently on ice for 1 h, followed by ultrafiltration (50 K mwco) until the volume was reduced from 12 to <0.5 mL, to remove any free unincorporated corrole and concentrate the particle mixture. Retentates (containing HerMn particles) were recovered and analyzed by absorbance spectroscopy to determine the corrole and protein concentrations in HerMn and resulting corrole:protein ratio in each HerMn preparation, which remained at approx. 30:1 M ratio after filtration (Table S1). The concentration used for cell treatment was based on the corrole concentration in each complex.

2.2. Particle sizing

A Malvern ZEN 3600 Zetasizer Nano was used for Dynamic Light Scattering (DLS) measurement. Samples were pipetted into a low volume quartz cuvette with appropriate concentrations to prevent

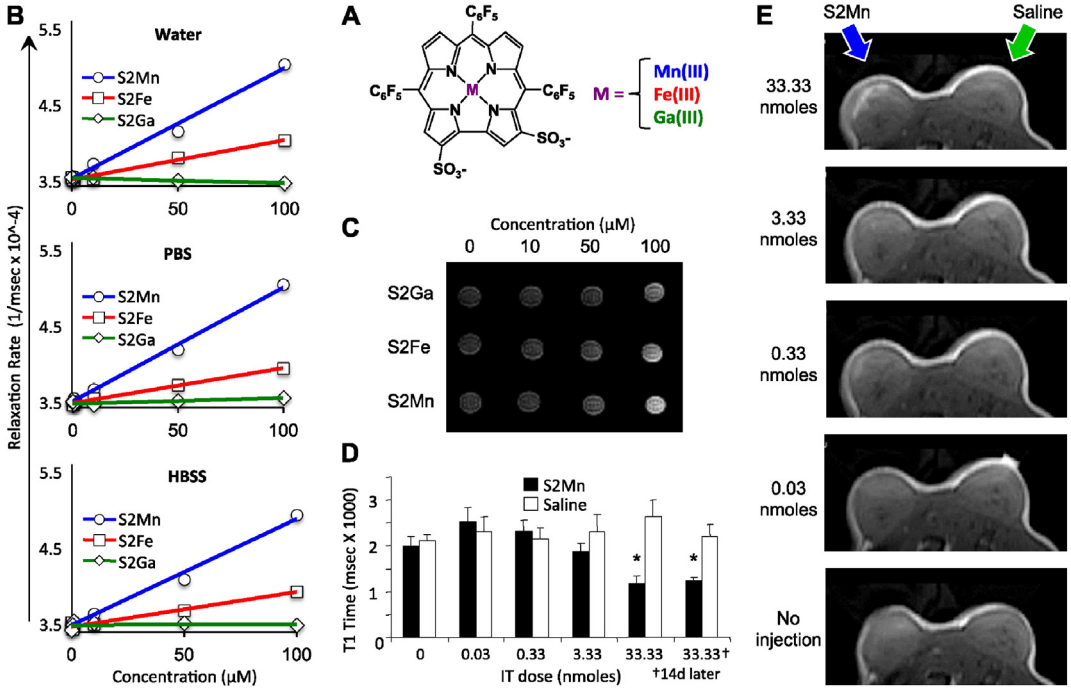

Fig. 1. Effect of Ga-, Fe-, and Mn- corroles on T1 relaxation rate and contrast change. A, Chemical structure of a metallated sulfonated corrole. S2Mn, S2Fe, and S2Ga are specified by replacement of metal ion (M) with Mn(III), Fe(III) or Ga(III), respectively. B–C, T1 relaxation times and contrast image of S2Mn, S2Fe, and S2Ga solutions *in vitro*. Graphs in B show T1 relaxation time measurements of indicated buffer solutions in Eppendorf tubes containing increasing concentrations of each corrole. N = 3 per concentration. Image in C shows the contrast change acquired from PBS containing indicated concentrations of corroles measured in B. D–E, T1 relaxation measurements and MRI of IT-injected tumors. Mice bearing HER2 + bilateral flank MDA-MB-435 tumors received IT injections of S2Mn in right tumors and equivalent volumes of saline in left tumors followed by (D) measurement of T1 change, and (E) MR image acquisition after delivery of indicated doses of S2Mn. In D, contralateral (left) tumors injected with saline are indicated by open bars. *, $p < 0.05$ as determined by t-test comparing S2Mn and saline. N = 8 different recovery intervals.

aggregation. Data shown represent the particle size distribution (PSD), which reports the most frequent particle size in the sample accounting for intensity fluctuations of larger particles. The PSD of each sample was acquired at ≥9 measurements/sample, with each measurement comprising 20 runs averaging 34,000 particle-counts/s. Intensity of particles was computed *via* Zetasizer Software version 7.01, which applies the Stokes-Einstein equation to correlate the change in the scattering intensity and particle movements.

2.3. Electron microscopy

Transmission electron microscopy (TEM) was performed using a TF20 (FEI Tecnai) transmitting electron microscope fitted with a field emission gun, operated at 200 kV. HerMn samples were prepared by dispersing the nanoparticles in hexane and dropping the solution onto an amorphous carbon coated grid. Images were obtained using a TIETZ F415MP CCD camera and processed using TIETZ Tomography package or ImageJ software.

2.4. Cells

MDA-MB-435 (HER2 + human ductal carcinoma) cell lines were obtained from the National Cancer Institute, and MDA-MB-231 (HER2- human mammary adenocarcinoma) and SKBR3 (HER2 + human mammary adenocarcinoma) cell lines were obtained from ATCC. BT-474 (HER2 + human ductal carcinoma) cells were a kind gift from Dr. Xiaojiang Cui (Cedars-Sinai Medical Center). Cell lines were maintained at 37 °C in complete media [Dulbecco's modified Eagle's medium (DMEM), 10% fetal bovine serum and 100 U/mL penicillin/100 μg/mL streptomycin] at 5% CO_2. We previously verified the relative cell surface levels of HER2 on these cells by ELISA under non-permeabilizing conditions [17].

Human cardiosphere-derived cells (CDCs) were prepared as described previously [18]. Briefly, endomyocardial biopsies from the right ventricular aspect of the interventricular septum were obtained from healthy hearts of deceased tissue donors. Heart biopsies were minced into small fragments and briefly digested with collagenase. Explants were then cultured on 20 mg/ml fibronectin (BD biosciences)-coated dishes. Stromal-like flat cells and phase-bright round cells grew out spontaneously from the tissue fragments and reached confluence by 2–3 weeks. These cells were then harvested using 0.25% trypsin (GIBCO) and cultured in suspension on 20 mg/ml poly d-lysine (BD Biosciences) to form self-aggregating cardiospheres. CDCs were obtained by seeding cardiospheres onto fibronectin-coated dishes and passaged. CDC cultures were maintained at 5% CO_2 at 37 °C, using IMDM basic medium (GIBCO) supplemented with 20% FBS (Hyclone), 1% penicillin/streptomycin, and 0.1 ml 2-mercaptoethanol. Human heart biopsy specimens, from which CDCs were grown, were obtained under a protocol approved by the institutional review board for human-subject research.

2.5. Cell toxicity assays

Indicated cells were plated at 10,000 cells/well in a 96-well dish. 48 h later, media was replaced with fresh complete media containing the indicated concentrations of HerMn, S2Mn, HerPBK10 or saline in 100 μL final volume/well. Plates were rocked for 4 h at 37 °C followed by further incubation without rocking for 20 h at 37 °C. Cell number was then determined by crystal violet (CV) assay as described previously [10]. Human CDCs were plated at 8000 cells per well in a 96-well dish. 48 h later, media was replaced with fresh complete media containing the indicated concentrations of HerPBK10, S2Mn, HerMn or doxorubicin, in 40 μL total volume/well. Plates were rocked for 4 h at 37 °C followed by supplementation with complete media to a 0.1 mL final total vol and continued incubation without rocking for 32 h at 37 °C. Cell survival was determined by MTS assay (Promega).

2.6. Mitochondrial membrane permeability assay

MDA-MB-435 cells were plated in Delta T chambers at 100,000 cells/chamber and incubated for 48 h. Media was replaced by 1 mL of fresh complete media containing the indicated concentrations of HerMn, S2Mn, HerPBK10 or PBS, followed by incubation for 24 h at 37 °C. Cells were then washed with Hank's Buffered Salt Solution (HBSS), and incubated in 30 nM tetramethylrhodamine methyl ester (TMRM; Invitrogen) in HBSS, 1 h at 37 °C. Images were acquired at different z-depths using laser scanning confocal microscopy. Mitochondrial membrane potential was quantified from a z-stacked maximum intensity projection of each acquired image by calculating the average fluorescence intensity for all cells in each field of view, from 3 independent experiments. TMRM has an excitation peak of 532 nm and an emission peak of 580 nm, so fluorescence was measured in the 550–620 nm range. The distribution of TMRM, a cationic dye, across the mitochondrial membrane is governed primarily by the Nernst equation [19], whereas transmembrane potential collapse results in its diffusion into the cytosol, thus reducing its intracellular fluorescence intensity [20].

2.7. Immunofluorescence

MDA-MB-435 cells were plated on coverslips in a 6-well dish at 100,000 cells/well and incubated for 48 h before media was replaced with 1 mL fresh media containing indicated concentrations of HerMn, S2Mn, HerPBK10 or PBS. Cells were incubated a further 24 h followed by fixation and processing for immunofluorescence as described previously [10]. Where indicated, cells were pre-incubated with 5 mM Tiron for 1 h before receiving HerMn. Specimens received anti- alpha-tubulin primary and Alexafluor 488 goat anti-mouse secondary antibodies (Invitrogen) at 1:100 and 1:1000 dilution in 1% BSA/PBS, respectively. Texas Red-X Phalloidin (Invitrogen) at 1:100 dilution was co-incubated with the secondary antibody, followed by incubation with 300 nM DAPI for 5 min before washing and mounting. Images were acquired using a Leica SPE laser scanning confocal microscope.

2.8. Animals

Nude (NU/NU) mice were obtained from Charles River Laboratories, Inc. All procedures involving mice were performed following Institutional of Animal Care and Use Committee (IACUC)-approved protocols in accordance with the institutional and national guide for the care and use of laboratory animals.

2.9. Tumor growth and monitoring in vivo

Female nude mice (NU/NU, 6 weeks; Charles River) received subcutaneous bilateral flank implants of 1×10^7 MDA-MB-435 human HER2 + cancer cells per implant. When average tumor sizes reached ~200 mm^3, mice were randomized and classified into 4 groups, each receiving daily injections for 6 sequential days of: HerMn or S2Mn at 5 nmoles corrole per injection; HerPBK10 at equivalent protein concentration to that of HerMn; or saline, which served as a mock-treatment control. Tumor volumes (height x width x depth) were measured manually by caliper. Data were analyzed using a one-way ANOVA followed by a Bonferroni post hoc test.

2.10. Xenogen imaging

HerPBK10 and BSA were separately labeled with Alexafluor-680 at primary amines and isolated from free, unconjugated dye by size exclusion chromatography using a commercial protein labeling kit, following manufacturer's protocol (LifeTechnologies). The labeled HerPBK10 or BSA was then combined with S2Mn to form HerMn or BSA-Mn particles, and processed by ultrafiltration as described earlier, which further removed any free dye and corrole molecules. The UV/Vis spectra of

retentates (containing particles) were obtained to calculate the concentration of corroles (see Table S1) and dye (184,000 $cm^{-1}M^{-1}$ extinction coefficient at 679 nm) in the HerMn or BSA-Mn sample. Protein concentration in the sample was determined by Bradford-based (Bio-Rad) protein assay. Mice bearing MDA-MB-435 flank tumors implanted as described earlier received 12 nmol of Alexafluor 680-labeled HerMn (total volume 125 μL), or BSA-Mn by tail vein injection, and immediately imaged at the indicated time points by a Xenogen Spectum imager using 640 nm excitation and 700 nm emission filters. After whole animal imaging, mice were sacrificed and tissues harvested for imaging using the same parameters, with images of all tissues from each mouse acquired simultaneously. Epifluorescence images were normalized to one another by adjusting the minimum fluorescence values to the same level before calculating average fluorescence intensities of the overall region of each selected tissue. Tissue fluorescence was graphed by normalizing the fluorescence of each tissue to the liver.

2.11. Magnetic resonance (MR) studies

A 9.4 T Bruker BioSpec 94/20 was used to assess T1 relaxation and contrast enhancement for *in vivo* studies involving IT injections and all *in vitro* studies. For *in vitro* studies, change in relaxation time was captured and analyzed using a RARE sequence with varying repetition times. The relaxation times were determined by least square fitting of the signal from the region of interest representing the different concentrations.

To determine the effect of cellular uptake on S2Mn or HerMn -mediated T1 relaxation time shortening, MDA-MB-435 cells were first detached from cell culture flasks using 2 mM EDTA in PBS and washed three times using PBS supplemented with 0.01% of Ca^{2+} and Mg^{2+}. 1×10^7 cells per sample were then incubated on ice for 30 min with 120 nM of S2Mn or HerMn (with respect to corrole concentration) to promote cell surface binding but not internalization. Cells were then warmed to 37 °C for 1 h to promote uptake, followed by washing three times with PBS to remove non-internalized S2Mn or HerMn. Cell pellets were suspended in 100 μL of PBS and subject to MRI as described earlier. Afterwards, cell lysates were prepared and assessed by absorbance spectroscopy to determine the concentration of internalized corrole.

For experiments involving intratumoral (IT) injections *in vivo*, nude mice with bilateral flank human HER2 + MDA-MB-435 tumors (size: ~95 mm^3) received IT injections of S2Mn at increasing concentrations (30 μL of 0, 1, 10, 100, and 1000 μM solutions), with each higher dose injected sequentially into the same tumor. Equivalent volumes of saline were injected into the contralateral tumor. T1 changes and T1-mapped images of the tumor regions were acquired after each injection by MRI. A different mouse bearing similar tumors received HerMn following a similar regimen. Specifically, IT injections were comprised of 100 μL of 500 μM HerMn delivered once per day for eight days. MRI was conducted immediately after the eighth injection. MRI signals were quantified by acquiring each image at eight different recovery intervals, producing an exponential recovery curve that was fit with a standard equation, $M_o = M_{inf}(1^{-e\text{-}RT/T1})$ where Mo = observed magnetization, M_{inf} = max polarization at infinite time, RT = delay time between the saturation and acquisition. Standard deviations were derived from least squared fitting of the data.

For experiments involving systemic delivery *in vivo*, nude mice bearing subcutaneous flank human HER2 + MDA-MB-435 tumors (size ~100 mm^3) received daily tail vein injections (100 μL/injection) of HerMn or S2Mn (each at 8 nmol corrole/injection), or saline for 8 days or 0.1 mmol/kg gadolinium (Optimark™ gadoversetamide) for 10 min prior to imaging. Mice were subjected to MRI utilizing a 7 T Bruker BioSpin 7 following the eighth injection. Imaging was performed using a T1-weighted spin-echo sequence, and 2D-acquisition with the following parameters: repetition time (TR) = 1000 ms, echo time (TE) = 9 ms, number of signal averages (NSA) = 2, 3 × 3 cm field of view (FOV), forty-six 0.5 mm-thick slices and a 334 μm in-plane resolution. Images were analyzed using online imaging analysis software (ImageJ) by measuring the signal intensity of several areas of each tumor, excluding the necrotic core. The measurements from each mouse were normalized by the signal intensity of nearby muscle tissue.

3. Results

3.1. Mn-corrole has the greatest effect on T1 relaxation rate and MRI contrast enhancement compared to Fe- and Ga-corroles

We screened several metallated corroles for their ability to augment T1 relaxation rates and MRI contrast in solution in order to select the best candidate for subsequent evaluation *in vivo*. Based on their paramagnetic potential, sulfonated manganese, iron, and gallium -metallated corroles (S2Mn, S2Fe, and S2Ga, respectively) were chosen for such comparisons (chemical structure shown in Fig. 1A). The T1 relaxation time shortening induced by each compound remained unchanged whether the solvent was water, phosphate buffered saline (PBS), or Hanks Balance Salt Solution (HBSS) (Fig. 1B). Of the three compounds measured, S2Mn, exhibited the largest T1 time shortening (Fig. 1B) and contrast enhancement (Fig. 1C) *in vitro*, and was selected for evaluation *in vivo*.

To determine the threshold of detecting S2Mn in tissue, we delivered known dosages of S2Mn at escalating concentrations directly into tumors on mice and monitored T1 relaxation shortening and corresponding contrast enhancement. Specifically, a mouse bearing subcutaneous bilateral flank tumors received intratumoral (IT) injections of either S2Mn at escalating doses or saline (in the contralateral tumor) followed by measurement of T1 time shortening and MR image acquisition, captured after each dose escalation. An IT accumulation of ≤3 nmoles S2Mn yielded no significant relaxation time reduction (Fig. 1D), and likewise produced no MRI contrast-enhancing signal (Fig. 1E). However, injection of 33 nmoles of S2Mn in the tumor yielded a significant difference in T1 time shortening compared to the equivalent volume of saline injected into the contralateral tumor (Fig. 1D) ($p < 0.05$), and could be measured in the same tumor up to two weeks after injection (Fig. 1D) ($p < 0.05$). Likewise, this dose produced a detectable MR contrast enhancement over saline at the injection site (Fig. 1E). Based on the approximate area of contrast detected in the tumor, a minimum threshold between 3 and 33 nmoles of Mn-corrole per ~100 mm^3 area of tissue is sufficient to yield tumor-to-tissue contrast enhancement, and provides a basis for determining the minimum *in situ* dosage required to yield a contrast signal.

3.2. HerMn assembly reduces corrole influence on T1 relaxation rate

We combined S2Mn with HerPBK10 in order to assemble complexes to test for targeting tumors after systemic delivery. Particle characterization included verifying the formation of protein–corrole assemblies and more importantly, assessing the effect of protein–corrole binding on T1 relaxation. To form particles, we combined S2Mn with HerPBK10 and filtered the resulting mixture to remove free corrole. The binding occurring between S2Mn and HerPBK10 was evidenced by corrole absorbance that remained in the retentate after filtration (Fig. 2A; "HerMn retentate"). The absorption spectrum of HerMn corresponded with that of free S2Mn that did not undergo ultrafiltration (Fig. 2A; "S2Mn unfiltered"), and contrasted with that of free corrole.

alone, which passed through the filter, and thus was not detected in the retentate (Fig. 2A; "S2Mn retentate"). The HerMn particles recovered from ultrafiltration retentates yielded an average diameter of 23.2 ± 1.81 nm, as detected by dynamic light scattering (Fig. 2B–C). These findings were confirmed by electron microscopy imaging and analysis, which showed that HerMn formed sphere-like particles that were approximately 20 nm in diameter (Fig. 2D). HerMn particles typically formed at a corrole:protein ratio of 30 ± 6 corrole molecules per HerPBK10 monomer (Table S1).

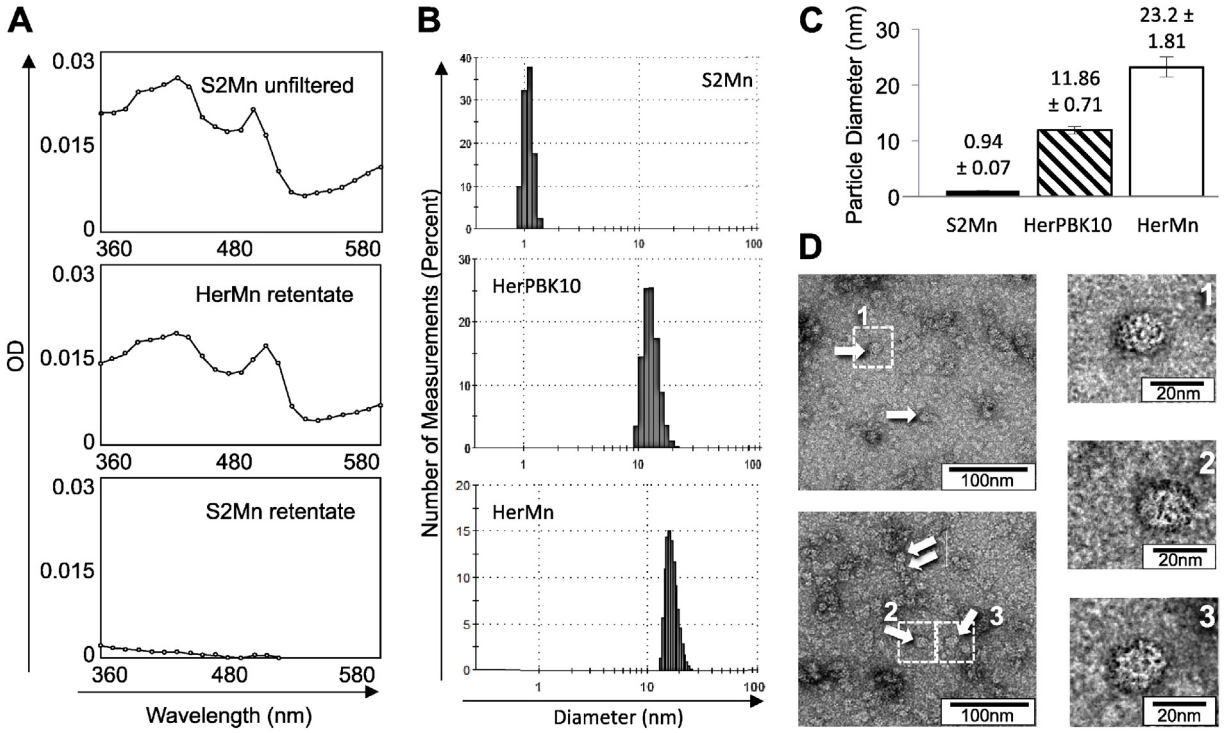

Fig. 2. Characterization of HerMn particle. A, Binding and retention of S2Mn to HerPBK10. S2Mn incubated −/+ HerPBK10 was subject to ultrafiltration. Retentates were recovered and analyzed by UV/Vis spectrophotometry. Absorbance curves show spectra of: "unfiltered S2Mn" (top panel); retentate of S2Mn incubated with HerPBK10 after filtration ("HerMn retentate"; middle panel); and, retentate of S2Mn alone after filtration ("S2Mn retentate"; bottom panel). B–C, Particle sizing of S2Mn, HerPBK10, and HerMn. Histograms in B show diameter (nm) and population distribution of S2Mn, HerPBK10, and HerMn particles in solution using dynamic light scattering (Zetasizer Nano, Malvern). Average diameters (nm) of corresponding particle populations are summarized in C. D, Electron microscopy of particles. Arrows highlight representative particles. Right panels show enlargements of boxed regions, and are contrast-enhanced to distinguish particle from background.

3.3. HerMn-enhanced T1 shortening and MRI contrast is activated by cell internalization

A comparison of HerMn and S2Mn in solution shows that particle formation considerably reduces the effect of the corrole on T1 relaxation rate (Fig. 3A). However, direct delivery of HerMn into tissue yields substantial tumor-to-tissue contrast enhancement (Fig. 3B) and significant T1 relaxation shortening (Fig. 3C) at the injection site. Taken together, these findings suggest that corroles are limited from interaction with water molecules in the intact HerMn particle but become solvent exposed upon tissue entry. To see if the low pH microenvironment of the tumor or endosomes facilitates corrole release and subsequent contrast

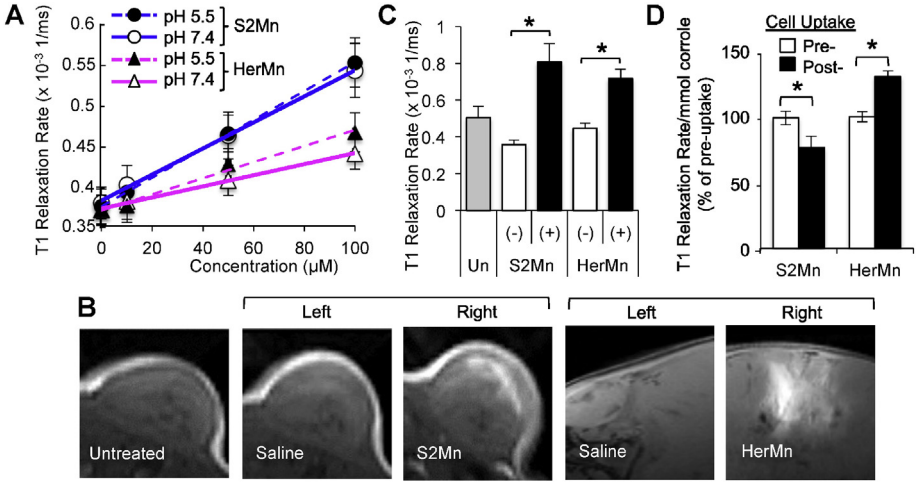

Fig. 3. Effect of tissue, pH, and cell uptake on HerMn-mediated T1 time and contrast change. A, Comparison of HerMn and S2Mn, and effect of pH on T1 relaxation in vitro. Increasing concentrations of S2Mn or HerMn were incubated in PBS, pH 7.4 or 5.5, for 30 min before T1 relaxation rates were measured by MR. N = 3 per concentration. B–C, MRI and T1 relaxation measurements of IT-injected tumors. Mice bearing HER2+ bilateral flank MDA-MB-435 tumors received daily IT injections of HerMn (50 nmoles/injection) (+) in the right flank tumor or saline (−) in the left flank tumor for 8 days. In (B), "Left" and "Right" refer to left and right flank tumors on the same mice. Tumor-to-tissue contrast (B) and corresponding T1 relaxation rates (C) were acquired after the final injection. IT injected tumors receiving 33.33 nmoles S2Mn and corresponding T1 time change (from Fig. 1D-E) are shown as a comparison. N = 8 different recovery intervals. D, Effect of cell uptake on T1 relaxation rate. T1 relaxation rates were obtained from S2Mn or HerMn samples in PBS alone or after uptake in MDA-MB-435 cells, representing Pre- and Post- cell uptake conditions, respectively. T1 relaxation rate changes were normalized by the concentration of corrole present in each condition (input corrole concentration for pre-cell uptake, and corrole concentration recovered from cell lysates for post-cell uptake). *, $p<0.05$ in C–D as determined by 2-tailed t-test.

enhancement, we incubated HerMn at pH 5.5 (mimicking the acid environment of late endosomes/lysosomes) [21]. These conditions did not significantly impact T1 relaxation rate of either S2Mn or HerMn solutions, in comparison to incubation at neutral pH (7.4) (Fig. 3A). Therefore, we examined the contribution of cell uptake on T1 relaxation.

S2Mn and HerMn were incubated on MDA-MB-435 cells in suspension under conditions promoting binding and internalization, and T1 relaxation rates were measured before and after uptake. Importantly, non-internalized particles were removed from cell surfaces before measuring relaxation time, and cells were quantified for internalized corroles afterward. After cell uptake, HerMn yielded a 31% T1 relaxation rate increase, whereas S2Mn alone mediated a 23% lower T1 relaxation rate (Fig. 3D). Together these findings indicate that cellular internalization but not acidic conditions trigger HerMn-enhanced T1 shortening.

3.4. HerMn-mediated tumor homing enables tumor-selective MRI in vivo

Before assessing the capacity of HerMn for *in vivo* MRI after systemic delivery, we first used optical imaging to evaluate its biodistribution. Mice bearing subcutaneous left flank MDA-MB-435 tumors received a single tail vein injection of fluorescently-labeled HerMn followed by optical image capture at sequential time points after delivery. Whole animal imaging shows that HerMn fluorescence accumulates in tumors immediately after intravenous (IV) delivery, and is retained in tumors up to 24 h later while circulating fluorescence is cleared from elsewhere in the body (Fig. 4A). Fluorescence images of tumors and organs harvested from sacrificed mice were compared to those from mice receiving Mn-corrole combined with labeled bovine serum albumin (BSA) to form a non-targeted control particle (BSA-Mn). HerMn exhibited preferential accumulation to the tumor with low (liver, kidney) to undetectable (heart, lung, spleen, skeletal muscle) distribution to non-tumor tissue (Fig. 4B–C). In contrast, BSA-Mn exhibited higher lung, kidney and spleen distribution and lower tumor accumulation compared to HerMn, while liver distribution was relatively similar (Fig. 4B–C).

The tumor-preferential biodistribution of HerMn suggests that the particle can facilitate sufficient tumor accumulation to enhance tumor-to-tissue contrast after systemic delivery. To test this, HER2 + −tumor bearing mice received daily IV injections of HerMn (8 nmoles per injection for 8 days) followed by MRI after the final injection. HerMn significantly enhanced contrast in tumors compared to non-tumor tissue (approximal muscle tissue) and in comparison to S2Mn, HerPBK10, and saline-treated groups (Fig. 4D–E). Additionally, mice treated with clinically-used doses of gadolinium produced similar levels of contrast enhancement as HerMn (Fig. 4D–E). However, it is important to note that whereas the Gd-treated mice were imaged immediately after Gd injection, the HerMn-treated mice (and additional controls) were imaged 24 h after the final injection. The prolonged retention of the particle in tumors could be advantageous over Gd, which is known to clear

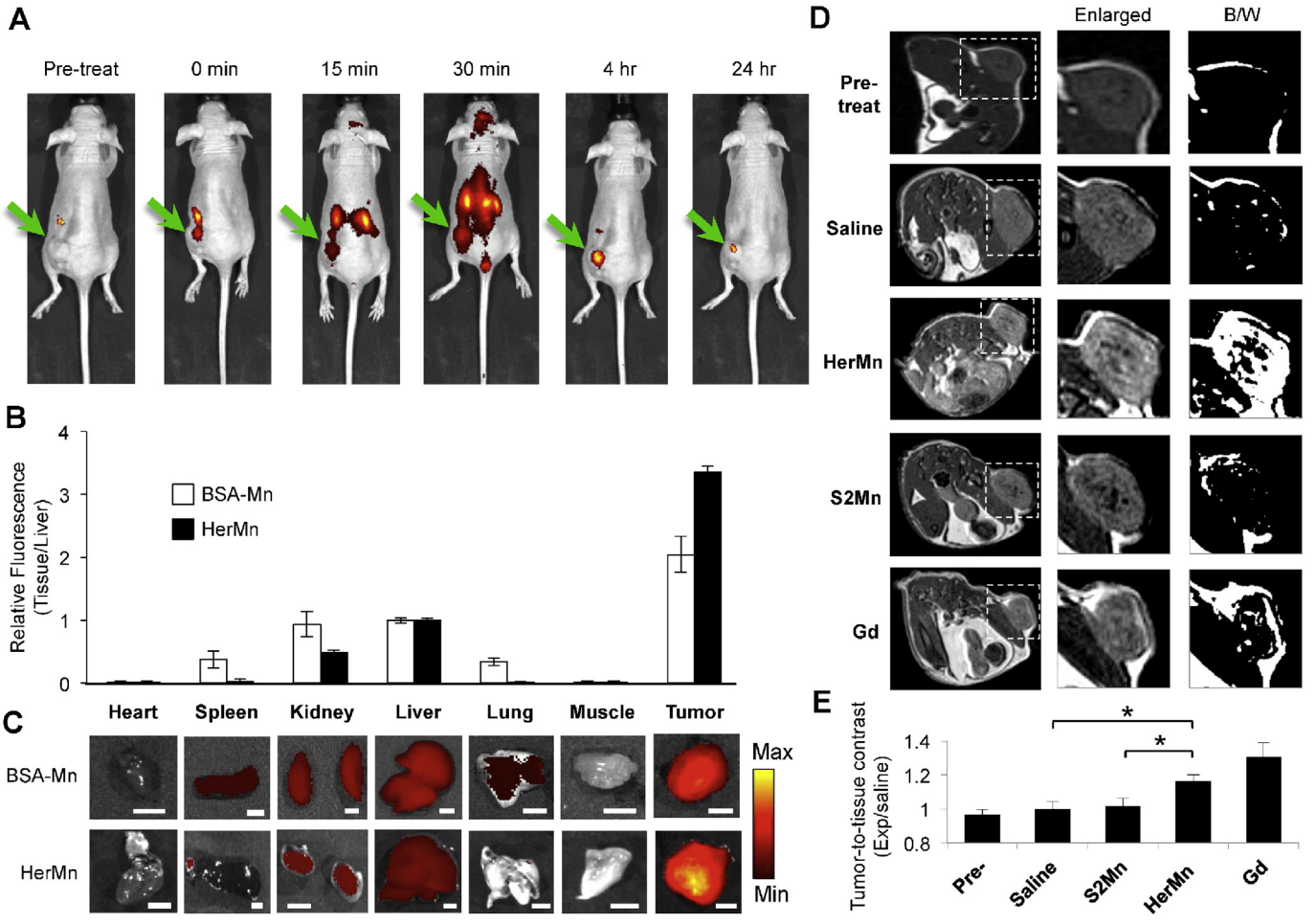

Fig. 4. Biodistribution and MRI after systemic delivery of HerMn. A–C, Biodistribution of HerMn. HER2+ tumor-bearing mice receiving an IV injection of fluorescently-labeled HerMn or BSAMn were (A) imaged live at the indicated time points. Tumors are indicated by arrows. B–C shows tissue distribution of HerMn from mice in A after the 24 h time point. Panels beneath bar graph show representative tissues (each from the same respective mouse) and fluorescences measured by the Xenogen imager. N ≥ 6 measurements per tissue. D, MRI after systemic delivery *in vivo*. Images (left panels) show cross-sections of tumor-bearing mice before and after receiving IV injections of HerMn, S2Mn, gadolinium (Gd; Optimark™ gadoversetamide), or saline. Tumors are delineated by boxed regions, which are enlarged in middle panels and rendered in black and white (B/W) mode (50% black and white pseudo-coloring) to highlight regions of contrast (right panels). E, MRI contrast comparisons between treatment groups *in vivo*. *, $p < 0.05$ as determined by t-test comparing HerMn and saline or HerMn and S2Mn. Saline, HerMn, S2Mn treatments: N = 5 measurements per tumor, per mouse (5 mice/group); Gd injected mice: N = 3 measurements per tumor per mouse (3 mice/group).

quickly after injection [22] and is consistent with our previous studies showing that HerPBK10-mediated delivery of a gallium-metallated corrole enabled tumor-retention of the molecule up to 30 days after injection [23].

3.5. Systemic delivery of HerMn is accompanied by tumor-toxicity

The systemic accumulation of HerMn in tumors led us to examine its effect on tumor growth and survival, especially in light of previous studies showing that the Mn-corrole can be cytoprotective [6,24]. Therefore, tumor-bearing mice receiving systemic HerMn (5 nmoles or 0.00022 mg/kg per day for 6 days) were monitored for tumor growth rates in comparison to control mice injected with either S2Mn, HerPBK10, or saline (average tumor size: 200 mm^3 at initiation of injections) (Fig. 5A). HerMn treatment resulted in a marked reduction in tumor volume, while HerPBK10 and S2Mn alone had no effect on tumor growth, similar to the mock (saline)–treated mice (Fig. 5B–C).

We also examined this on several tumor cell lines in culture by measuring overall viability of HER2+ (MDA-MB-435, SKBR3, and BT-474) and HER2- (MDA-MB-231) cells when exposed to escalating concentrations of either HerMn or the untargeted corrole, S2Mn. HerMn treatment resulted in concentration-dependent cell death in the HER2+ but not HER2- cells whereas the corrole alone (lacking a delivery agent) at equivalent concentrations did not affect viability (Fig. 5D). HerPBK10 alone is already known to have no effect on the viability of these cell lines [3,10,11,15]. Importantly, we found that at equivalent concentrations, HerMn elicits significantly greater cell death compared to clinically approved anti-HER2 therapies, trastuzumab, and trastuzumab/pertuzumab in combination (Fig. 5E).

As an assessment of clinical translatability and safety, we examined whether HerMn affects the viability of primary human cardiosphere-derived cells (CDCs). Unlike mouse myocardium, human myocardium is adversely impacted by HER2-targeted therapies currently used in the clinic, which exacerbate the cardiotoxicity of anthracycline-based therapies [25]. Cardiospheres are derived from endomyocardial biopsies obtained from healthy hearts of deceased tissue donors, and are comprised mainly of cardiomyocytes, endothelial cells, and smooth muscle cells [26], thus providing a reasonable representation of human cardiac tissue for *in vitro* studies. These cells express HER subunits at similar levels as human heart tissue [27]. Here, escalating concentrations of HerMn and individual components (HerPBK10 alone and S2Mn alone) had no detectable effect on CDC viability in contrast to doxorubicin (Dox) (Fig. 5F), which is known to cause acute myocardial cytotoxicity [28]. Microscopy shows cell rounding and lifting of Dox treated cells whereas HerMn caused no such morphological changes (Fig. 5G).

3.6. Targeted toxicity by HerMn is mediated by mitochondrial membrane disruption and oxidative damage to the cytoskeleton

The observed tumor-toxicity of HerMn was somewhat unexpected, as the Mn-corrole has exhibited cytoprotective effects on neuronal cells in previous studies [6,24,29]. Hence, we investigated the possible mechanisms contributing to HerMn-mediated tumor toxicity. Porphyrin-like compounds can be cytotoxic through mitochondrial

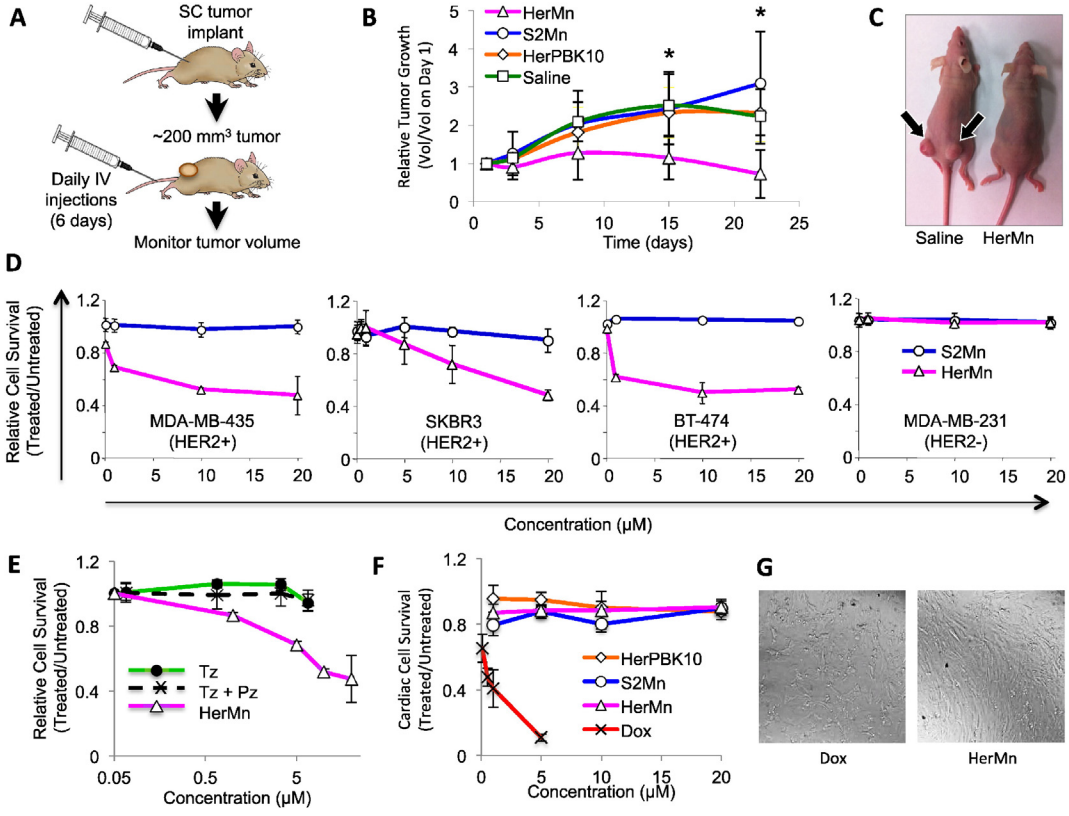

Fig. 5. Therapeutic efficacy of HerMn. A–C, Tumor growth after systemic delivery of HerMn. Regimen of tumor growth and treatment is shown in A. Tumor volumes (growth curves shown in B) were measured before (day 1), during (day 3), and after (days 8, 15, and 22) tail vein injections of indicated reagents. N = 8–10 tumors per group. *, $p < 0.05$ comparing HerMn *vs* each control group at day 15, and HerMn *vs* S2Mn at day 22 (several control animals required sacrifice from tumor burden, resulting in loss of power between the other two control groups and HerMn at day 22). Mouse image (C) shows comparison of tumor sizes of representative mice treated with saline or HerMn. D, Effect of HerMn on human HER2+ and HER2- tumor cell survival. Each cell line received the indicated concentrations of either HerMn or S2Mn and was subsequently assessed for cell survival 24 h later *via* crystal violet (CV) stain. N = 3 per concentration, from three separate experiments. E, Comparison to HER2-targeted therapies used in the clinic. MDA-MB-435 cells received the indicated concentrations of HerMn, trastuzumab (Tz) or trastuzuamb–pertuzumab combination (Tz + Pz) and were subsequently assessed for cell survival 48 h later *via* metabolic (MTS) assay. N = 3 per concentration, from 3 separate experiments. F–G, Human CDC viability after HerMn treatment. Human cardiosphere-derived cells (CDCs) received the indicated concentrations of either HerMn, S2Mn, HerPBK10, or doxorubicin (Dox) and were subsequently assessed for cell survival 48 h later *via* MTS assay. N = 3 per concentration, from three separate experiments. Images in G show unfixed CDCs under brightfield light after 2 days of incubation in 5 μM Dox or HerMn.

and cytoskeletal disruption, leading to apoptotic cell death [30]. In agreement, we have seen that a gallium-metallated corrole induces intracellular superoxide elevation, resulting in oxidative damage to the mitochondrial membrane and cytoskeleton [10]. To determine whether HerMn-mediated cytotoxicity is consistent with this, we examined the impact of HerMn on mitochondrial membrane potential by measuring its effect on uptake of the cationic dye, tetramethyl rhodamine methyl ester (TMRM). Mock (HBSS)–treated cells exhibited intense fluorescence indicative of dye accumulation in mitochondria, whereas 10 μM S2Mn alone slightly reduced this fluorescence intensity (Fig. 6A–B). In contrast, HerMn at equivalent and lower concentrations substantially reduced fluorescence intensity (Fig. 6A–B), and elicited a concentration-dependent loss of mitochondrial membrane potential (Fig. 6A). Importantly, the conditions of treatment allowed for the monitoring of mitochondrial function before cells became necrotic, as indicated by the retention of cell attachment to the substratum (Fig. 6B). An examination of cytoskeletal integrity showed that HerMn, but not HerPBK10 or S2Mn alone, caused breakdown of actin and microtubules, resulting in cytoplasmic collapse (Fig. 6C). Treating the cells with the oxygen scavenger, Tiron, before adding HerMn, preserved the cytoskeletal structure (Fig. 6C), suggesting that reactive oxygen species contribute to HerMn-mediated cytoskeletal disruption.

4. Discussion and conclusions

These studies demonstrate that a sulfonated manganese(III) corrole can be used as an MRI contrast-enhancing agent and induce cytotoxicity while retaining the high protein binding capability of corrole molecules. This latter feature has enabled the non-covalent assembly of HerMn, in which the tumor-targeting and penetration features of HerPBK10 are combined with the dual cytotoxic and paramagnetic properties of a manganese(III) corrole. The advantages of this particle over conventional contrast agents include its ability to target tumors, and impart both imaging and therapeutic activities. Importantly, these studies show that HerMn has improved toxicity to HER2+ tumor cells over the HER2-targeted signal-inhibitors, trastuzumab and pertuzumab, which are currently used in the clinic. Taken altogether, these findings suggest that HerMn may have potential clinical impact.

Selective targeting of HerMn to HER2+ but not HER2- tumor cells *in vitro* and significantly higher tumor-accumulation compared to a non-specific protein (BSA) bound to Mn-Corrole *in vivo* together indicate that active targeting, in contrast to enhanced permeability and retention (EPR), is a major contributor to the tumor homing observed here. These findings support our previous studies showing that HerPBK10 exhibits preferential targeting *in vivo* to tumors displaying

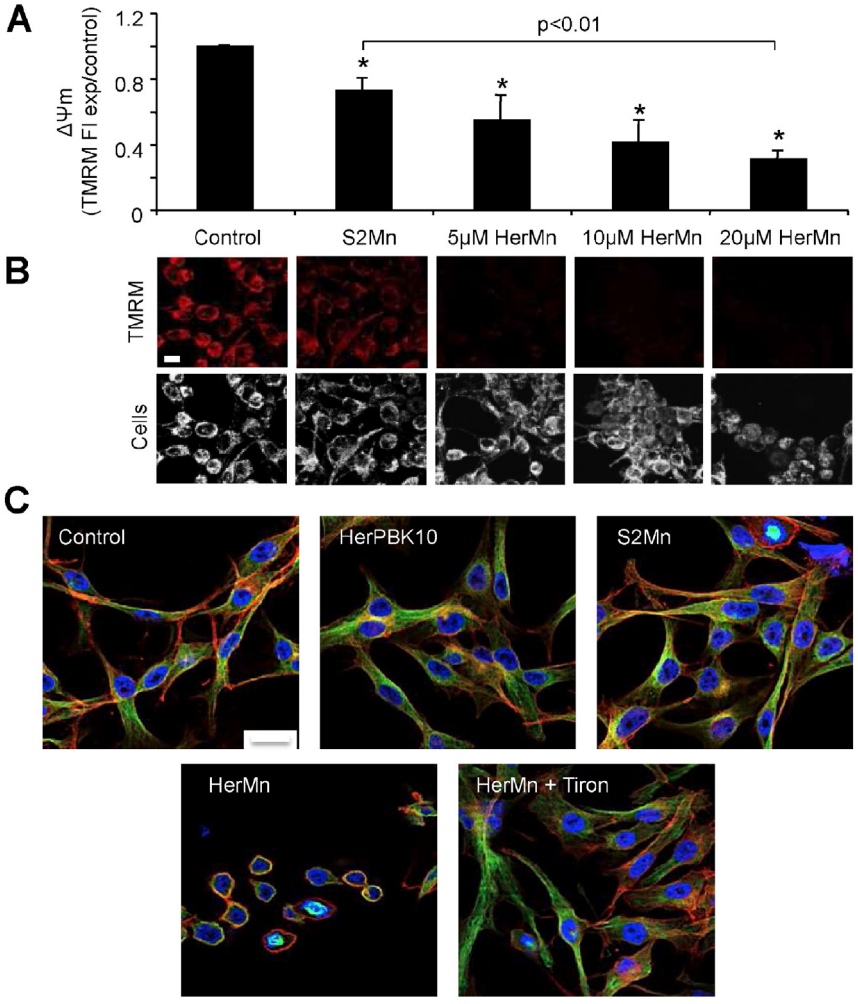

Fig. 6. Mechanism of HerMn cytotoxicity. A–B, Effect of HerMn on mitochondrial membrane potential (ΔΨm). MDA-MB-435 cells were treated with 10 μM S2Mn or HerMn at the indicated concentrations, and assessed for mitochondrial membrane integrity 24 h later by measurement of TMRM uptake. A, Measured quantum yield of TMRM fluorescence per cell from at ≥3 independent fields per experiment. Measurements are shown as the fluorescence intensity (FI) of experimental groups normalized by control (PBS) treatment. N = 3 experiments. *, $p < 0.01$ compared to control. B, Micrographs showing z-stacked maximum intensity projections of TMRM red fluorescence in cells treated with the indicated concentrations of reagents. Scale bar = ~10 μm. C, Effect of HerMn on the cytoskeleton. Micrographs show fluorescence labeling of actin (red) and tubulin (green) in HER2+ MDA-MB-435 cells after treatment for 24 h with HerMn or S2Mn (each at 5 μM corrole concentration), HerPBK10 (at equivalent protein concentration as HerMn) or PBS (control). Where indicated, cells received Tiron (5 mM) for one hour before HerMn treatment. Blue, nucleus. Scale bar = ~10 μm. Lower and higher magnification images are shown in Fig. S1.

relatively higher HER2-3 levels in contrast to those expressing low/negligible levels of HER2-3 [15]. Unlike gadolinium, which is known to clear quickly after injection [22], our data indicates that HerMn is retained to allow sufficient imaging even 24 h after injection. Thus it is possible to allow tumor accumulation over time to enable both imaging during or after treatments, and therapeutic efficacy.

The non-distribution and non-toxicity to heart tissue, especially in human cardiac tissue, presents a major advantage over traditional chemotherapy reagents such as anthracyclines, which have known cardiotoxic effects [28]. Previous studies show that the Mn-corrole is neuroprotective at low (≤1 μM) levels but toxic at higher concentrations [6], hence high local accumulation in tumors afforded by targeted delivery likely contributes to tumor toxicity while sparing heart tissue. Notably, HerMn appeared to transiently localize to the head region (15–30 min), which could result from either extra-cranial circulation or specific delivery to the brain. We are exploring the latter in separate studies, given that HER3 expression on brain endothelium mediates neuregulin transcytosis into brain parenchyma [31]. If confirmed, such findings could have important implications with regard to targeting metastatic tumors.

Our mechanistic studies on the gallium-metallated corrole nanoparticle, HerGa (comprising HerPBK10 and a sulfonated gallium-metallated corrole) show that endosomal escape is required for corrole-mediated cytotoxicity after cell entry [10]. Additionally, those studies show that the Ga-corrole induces superoxide elevation, causing oxidative damage to the mitochondrial membrane and cytoskeleton [10]. The mitochondrial membrane disruption and superoxide-mediated cytoskeletal collapse observed here suggest that HerMn acts through similar mechanisms, and is likely to also require cytoplasmic entry for accessing molecular targets of toxicity. One such target may be the translocator protein, TSPO, which mediates porphyrin passage into mitochondria and contributes to cellular homeostasis [32,33]. We have recently found that this molecule is a target of the gallium-metallated compound (manuscript in preparation). The elevation of this protein in cancer cells [34,35] may sensitize tumors to this and other metallated corroles, thus adding to tumor-selective toxicity.

The slower relaxation mediated by HerMn compared to S2Mn in solution suggests that corrole binding to HerPBK10 may constrain the interaction of manganese(III) centers with water molecules in the saline suspension. However, this does not seem to interfere with its contrast-enhancing capability *in vivo*, specifically in tissue, suggesting that the corroles in HerMn become solvent-exposed upon cell uptake. Such a feature would enable tumor-selective imaging and detection by combining targeting with internalization-triggered contrast enhancement. Our *in vitro* findings on cells in culture are consistent with this prediction and furthermore indicate that post-endocytic processes rather than acidic conditions of the endosome contribute to this. The latter feature is advantageous by avoiding the need for the particle to localize in late endosomes/lysosomes to release the corrole, which would otherwise mitigate its therapeutic effect. This additionally avoids premature release of the contrast agent under acidic environments outside of the tumor or conversely retention of the contrast agent if the particle remains in a neutral intracellular compartment, which would both confound imaging analysis and interpretation. Taken together with the earlier systemic delivery results, these studies show that HerMn enables tumor-selective detection through both targeting and activatable T1-relaxation shortening triggered by cell uptake.

Collectively, the multifunctional features of each component comprising HerMn contribute to its translational potential as a tumor-targeted therapeutic agent with clinically-relevant imaging capabilities as well as activatable, tumor-selective detection.

Acknowledgments

This research was supported by grants to LKMK from the NIH/NCI (R01 CA140995 and R01 CA129822), and from the National Center for Research Resources, Grant UL1RR033176, which is now at the National Center for Advancing Translational Sciences, Grant UL1TR000124. The authors are grateful to IC Atanasov, X Zhang, LS Lam, and H Zhou at the Electron Imaging Center for NanoMachines (EICN) within the California NanoSystems Institute (CNSI) at UCLA for EM services and assistance; and acknowledge the use of instruments within the EICN supported by the NIH (1S10RR23057 to ZHZ) and CNSI at UCLA. The authors also thank X Da and W Tawackoli of the Cedars-Sinai Imaging Core for Xenogen imaging services provided for this study. Finally, we thank the University of Wisconsin–Madison Biochemistry MediaLab for use of mouse clipart. JDS thanks A Rozenek and JR Sims for their support and inspiration; and LKMK thanks C Rey, MM-Kauwe, and D Revetto for unwavering support and guidance. ZG thanks the Israel Science Foundation (Grant No. 274/13) for financial support of work performed at the Technion. IH, GK, KS, RAM thank the Radiology Research Endowment Fund and the Small Animal Imaging Core at the Saban Research Instititute.

Appendix A. Supplementary data

Supplementary data to this article can be found online at http://dx.doi.org/10.1016/j.jconrel.2015.08.046.

References

[1] A. Fernandez-Fernandez, R. Manchanda, A.J. McGoron, Theranostic applications of nanomaterials in cancer: drug delivery, image-guided therapy, and multifunctional platforms, Appl. Biochem. Biotechnol. 165 (7–8) (2011) 1628–1651.
[2] M.P. Melancon, R.J. Stafford, C. Li, Challenges to effective cancer nanotheranostics, J. Control. Release 164 (2) (2012) 177–182.
[3] H. Agadjanian, et al., Specific delivery of corroles to cells via noncovalent conjugates with viral proteins, Pharm. Res. 23 (2) (2006) 367–377 (Epub 2006 Jan 2019).
[4] A. Mahammed, I. Goldberg, Z. Gross, Highly selective chlorosulfonation of tris(pentafluorophenyl)corrole as a synthetic tool for the preparation of amphiphilic corroles and metal complexes of chiral planarity, Org. Lett. 3 (2001) 3443–3446.
[5] A. Mahammed, H.B. Gray, J.J. Weaver, K. Sorasaenee, Z. Gross, Amphiphilic corroles bind tightly to human serum albumin, Bioconjug. Chem. 15 (2004) 738–746.
[6] A. Kanamori, M.M. Catrinescu, A. Mahammed, Z. Gross, L.A. Levin, Neuroprotection against superoxide anion radical by metallocorroles in cellular and murine models of optic neuropathy, J. Neurochem. 114 (2) (2010) 488–498.
[7] H. Agadjanian, et al., Tumor detection and elimination by a targeted gallium corrole, Proc. Natl. Acad. Sci. U. S. A. 106 (15) (2009) 6105–6110.
[8] J.Y. Hwang, et al., Photoexcitation of tumor-targeted corroles induces singlet oxygen-mediated augmentation of cytotoxicity, J. Control. Release 163 (3) (2012) 368–373.
[9] J.Y. Hwang, et al., Investigating photoexcitation-induced mitochondrial damage by chemotherapeutic corroles using multimode optical imaging, J. Biomed. Opt. 17 (1) (2012) 015003.
[10] J.Y. Hwang, et al., A mechanistic study of tumor-targeted corrole toxicity, Mol. Pharm. 8 (6) (2011) 2233–2243.
[11] H. Agadjanian, et al., Tumor detection and elimination by a targeted gallium corrole, Proc. Natl. Acad. Sci. U. S. A. 106 (15) (2009) 6105–6110 (Epub 2009 Apr 6102).
[12] A. Rentsendorj, et al., Typical and atypical trafficking pathways of Ad5 penton base recombinant protein: implications for gene transfer, Gene Ther. 13 (10) (2006) 821–836.
[13] L.K. Medina-Kauwe, M. Maguire, N. Kasahara, L. Kedes, Non-viral gene delivery to human breast cancer cells by targeted Ad5 penton proteins, Gene Ther. 8 (2001) 1753–1761.
[14] M. Alimandi, et al., Cooperative signaling of ErbB3 and ErbB2 in neoplastic transformation and human mammary carcinomas, Oncogene 10 (9) (1995) 1813–1821.
[15] H. Agadjanian, et al., Chemotherapy targeting by DNA capture in viral protein particles, Nanomedicine 7 (3) (2012) 335–352.
[16] L.K. Medina-Kauwe, Development of adenovirus capsid proteins for targeted therapeutic delivery, Ther. Deliv. 4 (2) (2013) 267–277.
[17] H. Agadjanian, et al., Chemotherapy targeting by DNA capture in viral protein particles, Nanomedicine 7 (3) (2012) 335–352.
[18] R.R. Makkar, et al., Intracoronary cardiosphere-derived cells for heart regeneration after myocardial infarction (CADUCEUS): a prospective, randomised phase 1 trial, Lancet 379 (9819) (2012) 895–904.
[19] R.C. Scaduto Jr., L.W. Grotyohann, Measurement of mitochondrial membrane potential using fluorescent rhodamine derivatives, Biophys. J. 76 (1 Pt 1) (1999) 469–477.
[20] V. Dall'Asta, et al., Membrane potential changes visualized in complete growth media through confocal laser scanning microscopy of bis-oxonol-loaded cells, Exp. Cell Res. 231 (2) (1997) 260–268.
[21] L.K. Medina-Kauwe, J. Xie, S. Hamm-Alvarez, Intracellular trafficking of nonviral vectors, Gene Ther. 12 (24) (2005) 1734–1751.
[22] S. Aime, P. Caravan, Biodistribution of gadolinium-based contrast agents, including gadolinium deposition, J. Magn. Reson. Imaging 30 (6) (2009) 1259–1267.

[23] J.Y. Hwang, et al., Photoexcitation of tumor-targeted corrole induces singlet oxygen-mediated augmentation of cytotoxicity, J. Control. Release (2012) (in press).
[24] L. Kupershmidt, et al., Metallocorroles as cytoprotective agents against oxidative and nitrative stress in cellular models of neurodegeneration, J. Neurochem. 113 (2) (2010) 363–373.
[25] D.J. Slamon, et al., Use of chemotherapy plus a monoclonal antibody against HER2 for metastatic breast cancer that overexpresses HER2, N. Engl. J. Med. 344 (11) (2001) 783–792.
[26] L. Barile, et al., Human cardiospheres as a source of multipotent stem and progenitor cells, Stem Cells Int. 2013 (2013) 10.
[27] A.S. Barth, et al., Functional impairment of human resident cardiac stem cells by the cardiotoxic antineoplastic agent trastuzumab, Stem Cell Transl. Med. 1 (4) (2012) 289–297.
[28] D.L. Keefe, Anthracycline-induced cardiomyopathy, Semin. Oncol. 28 (4 Suppl. 12) (2001) 2–7.
[29] Z. Okun, et al., Manganese corroles prevent intracellular nitration and subsequent death of insulin-producing cells, ACS Chem. Biol. 4 (11) (2009) 910–914.
[30] S.D. Ferreira, et al., Analysis of mitochondria, endoplasmic reticulum and actin filaments after PDT with AlPcS(4), Lasers Med. Sci. 18 (4) (2004) 207–212 (Epub 2004 Jan 2014).
[31] A.J. Kastin, V. Akerstrom, W. Pan, Neuregulin-1-beta1 enters brain and spinal cord by receptor-mediated transport, J. Neurochem. 88 (4) (2004) 965–970.
[32] A. Verma, J.S. Nye, S.H. Snyder, Porphyrins are endogenous ligands for the mitochondrial (peripheral-type) benzodiazepine receptor, Proc. Natl. Acad. Sci. U. S. A. 84 (8) (1987) 2256–2260.
[33] P. Casellas, S. Galiegue, A.S. Basile, Peripheral benzodiazepine receptors and mitochondrial function, Neurochem. Int. 40 (6) (2002) 475–486.
[34] Austin CJ, Kahlert J Fau-Kassiou M, Kassiou M Fau-Rendina LM, & Rendina LM (The translocator protein (TSPO): a novel target for cancer chemotherapy. 1878–5875 (Electronic).
[35] X. Wu, K.A. Gallo, The 18-kDa translocator protein (TSPO) disrupts mammary epithelial morphogenesis and promotes breast cancer cell migration, PLoS One 8 (8) (2013), e71258.